



Journal of Geophysical Research: Earth Surface

RESEARCH ARTICLE

10.1002/2014JF003275

Kev Points:

- Phase-sensitive radar measures vertical ice velocities within ice divides
- Theoretical predictions of ice flow patterns around ice divide are confirmed
- Results provide strong evidence that power law ice rheologies are incomplete

Correspondence to: J. Kingslake, jonngs@bas.ac.uk

Citation

Kingslake, J., R. C. A. Hindmarsh, G. Aðalgeirsdóttir, H. Conway, H. F. J. Corr, F. Gillet-Chaulet, C. Martín, E. C. King, R. Mulvaney, and H. D. Pritchard (2014), Full-depth englacial vertical ice sheet velocities measured using phase-sensitive radar, J. Geophys. Res. Earth Surf., 119, doi:10.1002/2014JF003275.

Received 11 JUL 2014 Accepted 11 NOV 2014 Accepted article online 14 NOV 2014

Full-depth englacial vertical ice sheet velocities measured using phase-sensitive radar

Jonathan Kingslake¹, Richard C. A. Hindmarsh¹, Guðfinna Aðalgeirsdóttir², Howard Conway³, Hugh F. J. Corr¹, Fabien Gillet-Chaulet^{4,5}, Carlos Martín¹, Edward C. King¹, Robert Mulvaney¹, and Hamish D. Pritchard¹

¹British Antarctic Survey, Natural Environment Research Council, Cambridge, UK, ²Institute of Earth Sciences, University of Iceland, Reykjavík, Iceland, ³Department of Earth and Space Sciences, University of Washington, Seattle, Washington, USA, ⁴CNRS, Laboratoire de Glaciologie et Géophysique de l'Environnement, Grenoble, France, ⁵Laboratoire de Glaciologie et Géophysique de l'Environnement, Universite Grenoble Alpes, Grenoble, France

Abstract We describe a geophysical technique to measure englacial vertical velocities through to the beds of ice sheets without the need for borehole drilling. Using a ground-based phase-sensitive radio echo sounder (pRES) during seven Antarctic field seasons, we measure the temporal changes in the position of englacial reflectors within ice divides up to 900 m thick on Berkner Island, Roosevelt Island, Fletcher Promontory, and Adelaide Island. Recorded changes in reflector positions yield "full-depth" profiles of vertical ice velocity that we use to examine spatial variations in ice flow near the divides. We interpret these variations by comparing them to the results of a full-Stokes simulation of ice divide flow, qualitatively validating the model and demonstrating that we are directly detecting an ice-dynamical phenomenon called the Raymond Effect. Using pRES, englacial vertical ice velocities can be measured in higher spatial resolution than is possible using instruments installed within the ice. We discuss how these measurements could be used with inverse methods to measure ice rheology and to improve ice core dating by incorporating pRES-measured vertical velocities into age modeling.

1. Introduction

Mapping surface velocities of entire ice sheets remotely and repeatedly using satellites has advanced understanding of many aspects of ice sheet dynamics [e.g., Rignot et al., 2011; Rignot and Mouginot, 2012]. By comparison, measurements of the velocity of ice within glaciers and ice sheets are limited. Measuring englacial velocities can help date ice cores [Dansgaard et al., 1982; Raymond, 1983; Zumberge et al., 2002; Parrenin et al., 2007a, 2007b] and quantify ice rheology [Gillet-Chaulet et al., 2011; Pettit et al., 2011]. Previous studies have measured englacial velocities in glacier ice and firn using strain gauges and inclinometers installed in boreholes [e.g., Perutz, 1949; Raymond et al., 1994; Hawley et al., 2002; Zumberge et al., 2002; Elsberg et al., 2004; Pettit et al., 2011]. Installing such instruments requires time-consuming borehole drilling, so application of these methods has been limited spatially.

Gillet-Chaulet et al. [2011] measured englacial velocities using a surface-based geophysical technique not requiring drilling. Along two 20 km survey lines crossing ice divides on the Greenland ice sheet, they used a phase-sensitive radio echo sounder (pRES) [Corr et al., 2002] to retrieve high-resolution vertical velocity profiles covering the top ~40% of the ice sheet's thickness. They used these in situ velocity measurements to infer the rheological properties of ice using an ice-dynamical phenomenon that dominates ice flow near ice divides.

In these regions, where surface slopes and driving stresses are small, theory predicts that ice at depth "stiffens" owing to the nonlinear stress dependence of effective viscosity [Raymond, 1983]. This is known as the Raymond Effect [e.g., Martín et al., 2006; Gillet-Chaulet and Hindmarsh, 2011; Gillet-Chaulet et al., 2011], and, crucially for detecting the phenomenon using pRES, it reduces the englacial vertical velocity of ice near divides in comparison to flank regions [e.g., Nereson and Waddington, 2002; Vaughan et al., 1999; Nereson and Raymond, 2001; Pettit and Waddington, 2003; Pettit et al., 2007, 2011].

Several studies have examined this phenomenon theoretically. It was first predicted by *Raymond* [1983] using a numerical ice flow model and subsequent modeling studies have examined how temperature [*Hvidberg*, 1996; *Nereson and Waddington*, 2002], ice divide migration [*Nereson and Waddington*, 2002; *Martín et al.*,

1



2009b], basal sliding [Pettit et al., 2003; Martín et al., 2009b], and ice fabric [Martín et al., 2009a; Pettit et al., 2007, 2011] influence the Raymond Effect.

Indirect evidence of the Raymond Effect is contained in the pattern of radar-detected internal layers at ice divides. The reduced vertical velocities near the divide compared with the flanks results in anticlines, or "Raymond Arches" near the divide [e.g., Vaughan et al., 1999; Nereson and Raymond, 2001; Pettit and Waddington, 2003]. Analyses of the shape of these structures can be used to constrain the timing of ice divide formation [e.g., Conway et al., 1999; Martín et al., 2006] and migration [e.g., Price et al., 2007] and inform ice core site selection [Raymond, 1983; Drews et al., 2013].

Knowledge of englacial ice velocities can help to date ice cores. Ideally, dating is done by counting annual variations in ice core properties, but due to cumulative vertical compression this technique is often impossible near the bed, particularly in parts of the Antarctic where layers are barely distinguishable [Parrenin et al., 2007a, 2007b]. Here the age of the ice can be modeled between chemically distinctive layers of known age, but this requires a description of englacial vertical ice velocities [e.g., Dansgaard et al., 1982; Parrenin et al., 2007a, 2007b; Martín et al., 2014]. Current modeled ice core chronologies [e.g., Parrenin et al., 2007a, 2007b] often use analytical approximations of ice flow [e.g., Dansgaard and Johnsen, 1969; Lliboutry, 1979]. This introduces uncertainty that could be reduced by instead incorporating measured vertical velocities into age modeling.

Here we present results of pRES surveys conducted near ice divides at four sites in West Antarctica to measure englacial vertical velocities through to the bed of ice up to ~900 m thick. Such "full-depth" profiles are useful because we can reference them to the stationary bed to calculate absolute velocities. Without a full-depth profile velocities must be referenced to the ice surface or an internal layer, neither of which are stationary. The technique does not require borehole drilling and therefore allows mapping of englacial ice flow in higher spatial resolution than has previously been possible. We qualitatively compare our data to the results of a full-Stokes numerical ice flow model, showing that we are directly observing the Raymond Effect. We also fit our observations with two analytical ice flow approximations used in ice core dating to examine their ability to describe the observed ice flow.

In section 2 we describe the design and operation of pRES, our four field surveys, and the setup of the numerical model. In section 3 we discuss the physics of the Raymond Effect with reference to the results of a model simulation. In section 4 we present measured vertical velocity profiles and strain rate patterns and qualitatively compare these data to the predictions of the numerical model and analytical approximations. We discuss our results and their implications in section 5.

2. Methods and Field Surveys

2.1. The Design and Operation of the Phase-Sensitive Radio Echo Sounder

We calculate vertical ice velocities from time-separated measurements of the elevation of internal radar reflectors. To circumvent the restrictions on the total transmitted energy suffered by pulsed-radar systems and to increase the precision of reflector location by recording the phase of returns, pRES is designed as a step-frequency radar [Nye et al., 1972; Corr et al., 2002; Jenkins et al., 2006; Gillet-Chaulet et al., 2011]. Instead of transmitting a single pulse and recording the response of the ice as a time series, a network analyzer connected to two identical antennas is used to sample the frequency response of the ice, which is later converted to the time domain to detect reflectors. The network analyzer is located in a temperaturecontrolled box on a sledge between the two antennas, which are placed 7 m apart. Measurements are made with the antennas oriented either perpendicular or parallel to survey lines.

We follow the measurement and processing procedures described by Corr et al. [2002]. The frequency response of the ice is sampled at 1000+ equally spaced frequency steps, centered on 305 MHz (corresponding to a wavelength $\lambda \approx 0.6\,\mathrm{m}$ in ice). At each frequency step, one antenna transmits a monochromatic radio wave while the other antenna records the amplitude and phase of the response. The complex ratio of the received and transmitted signals at each step is recorded by the network analyzer. We use a total bandwidth, $B=160\,\mathrm{MHz}$ and an interval between frequency steps, Δf , between 50 and 100 kHz. With these settings, a full sweep of frequencies takes around 5 min to complete.

This sampling procedure yields the complex frequency domain of the radar response, which we convert to the time domain to yield time series of amplitude and phase using an inverse Fourier transform and a



constant radar wave velocity in ice $(168\,\text{m}\,\mu\text{s}^{-1})$ [Corr et al., 2002]. An algorithm detects reflectors on the basis of their brightness and phase uniformity and for each reflector calculates the difference in the phase recorded during two time-separated deployments (relative to a bright reflector that can be unequivocally located in both returns and lies beneath the firn layer at ~100 m depth). Although ignoring the density dependence of the radar wave velocity introduces an offset in reflector locations associated with the low-density firn layer, by assuming that the density of the ice below this bright reflector does not change between deployments, firn densification has no influence on measured phase differences. Finally, we convert this phase difference to a displacement and the time between deployments is used to calculate the vertical velocity of each reflector. We collate these measurements into vertical velocity profiles.

Although the resolution with which we can measure the range to a reflector, with $B=160\,\mathrm{MHz}$, is $\sim\!0.53\,\mathrm{m}$, the resolution with which we can detect reflector displacement is enhanced by taking into account the phase. However, this depends on the signal-to-noise ratio (SNR). Theoretically, in regions where the SNR is high, we can detect phase differences of 1° and relative reflector displacements can be detected to within $<1\,\mathrm{mm}$. However, because the phase is used to locate reflectors, there is a limit on the displacement that this technique can measure, which is related to λ . If a reflector detected in the first pRES return moves (relative to the bright reflector at $\sim\!100\,\mathrm{m}$ depth) further than λ ($\approx\!0.6\,\mathrm{m}$), the algorithm used to detect reflectors can fail to correctly identify the same reflector in the repeat return, leading to phase-unwrapping errors and large unphysical gradients in vertical velocity.

How accurately we can measure vertical velocities also depends on how accurately the radar system can be repositioned during return deployments. It is presently unclear how strong this dependence is, so using bamboo stakes placed during the initial deployment, the sledge and antennas are repositioned to within ~10 cm horizontally. Accurate repositioning may be more important in areas with strong horizontal variation in reflector and bed elevations.

We estimate the uncertainty in velocity measurements using the SNR of each reflector recorded in each deployment. We combine the phasor (a vector whose length and orientation represent the magnitude and phase of a signal) of each reflector with a noise phasor, which has a length equal to the median strength of the entire return and an unknown orientation. The uncertainty in the phase (which provides the uncertainty in each reflector's position) is defined as the deviation in the phase introduced by the noise phasor when it is oriented perpendicular to the reflector phasor. A conservative estimate of uncertainty in the velocity is calculated from the sum of the uncertainties in each reflector's position. Uncertainties calculated in this way vary with depth and between field locations because they depend on the strength of reflectors, noise levels and the rate of absorption. The median uncertainty calculated at a normalized depth of 0.5 from all the data presented below is $\sim 1.8 \, \mathrm{cm \ a^{-1}}$.

2.2. Field Surveys

We conducted pRES surveys at four field sites: an ice divide on Berkner Island, located between the Filchner and Ronne ice shelves (Figure 1a), an ice divide on Roosevelt Island in the Ross Ice shelf (Figure 1b), a triple junction (a location where three ice divides intersect) on Fletcher Promontory in the southwest Ronne Ice Shelf between Carlson Inlet and the Rutford Ice Stream (Figure 1c) and an ice divide on the Fuchs Piedmont Glacier on Adelaide Island (Figure 1d). The locations of our pRES survey stakes are indicated by the red and yellow points in Figure 1. Shown in blue are the locations of low-frequency (2–7 MHz) pulse-echo ice-penetrating radar surveys to image the bed and internal radar layer structure at each of the sites [Hindmarsh et al., 2011].

The Berkner Island, Roosevelt Island, and Adelaide Island pRES surveys were designed to investigate quasi-plane ice flow found in these locations. Hence, we surveyed lines of stakes (41 at Berkner, 35 on Roosevelt, and 33 on Adelaide) approximately centered on and running perpendicular to divide ridges (Figures 1a, 1b, and 1d). On Berkner Island and Roosevelt Island the stakes were arranged so that their density was larger near the divide. The slight misplacement of the high-density region in the Berkner Island survey and the misalignment of the Adelaide Island survey are due to very low surface gradients that are typical near divides. Fletcher Promontory contains complex three-dimensional radar layer structure [Hindmarsh et al., 2011], so our pRES survey reflected this (Figure 1c): 104 stakes were arranged in lines emanating from the triple junction's summit along two divide ridges and along the thalwegs of two interdivide troughs.

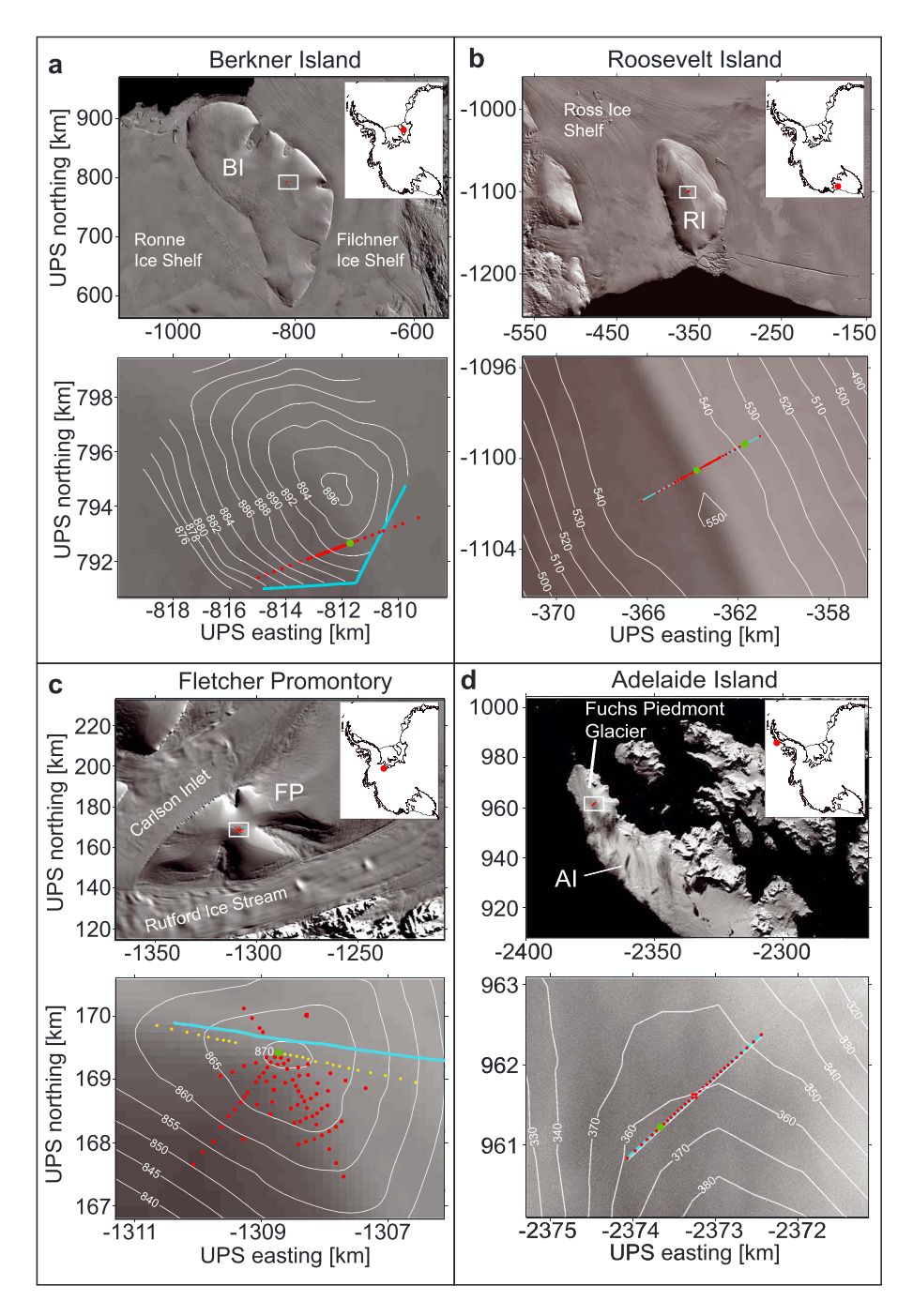


Figure 1. Our field sites and radar surveys. (a) The Berkner Island (BI) triple junction, (b) Roosevelt Island (RI) ice divide, (c) the Fletcher Promontory (FP) triple junction, and (d) the Fuchs Piedmont ice divide on Adelaide Island (AI). In the upper maps the insets show each site's location in West Antarctica, and the white boxes indicate regions enlarged in the lower maps, where red and yellow points indicate pRES stakes and the blue lines indicate low-frequency radar lines. White contours show surface elevations extracted from low-frequency radar surveys [*Hindmarsh et al.*, 2011] in Figures 1a and 1c and the BEDMAP2 data set in Figures 1b and 1d [*Fretwell et al.*, 2013]. Background images are from the Moderate Resolution Imaging Spectroradiometer mosaic of Antarctica [*Haran et al.*, 2005]. Coordinates and projection are polar stereographic with latitude of true scale 71°S.

After the first deployment at each location, we returned to make repeat measurements at Berkner Island after 2 years, Roosevelt Island after 3 years, Fletcher Promontory after 1 year, and Adelaide Island after 3 months. The short time separation of deployments on Adelaide Island was possible owing to high vertical velocities caused by high accumulation rates, while the long separation between deployments on Roosevelt Island was due to poor weather conditions, which prevented an earlier return.

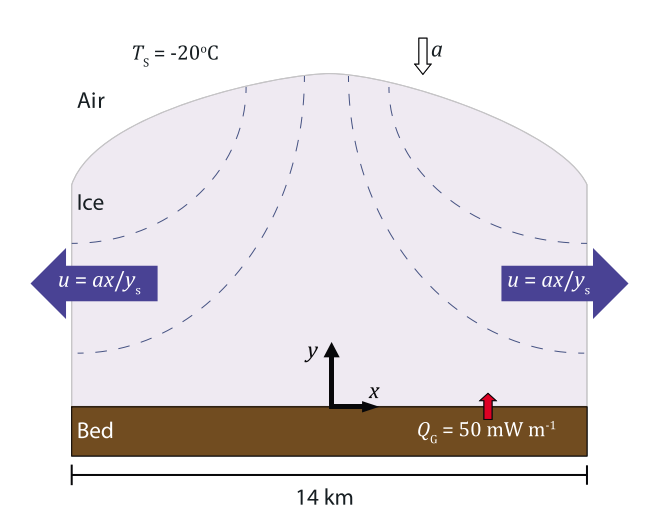


Figure 2. Geometry of the ice divide flow model.

At all four field sites we made multiple measurements at each stake with the antennas orientated either parallel or perpendicular to each survey line. Two different antenna orientations were used so that in future work our data may be used to detect signatures of anisotropy in the orientation of ice crystals that is expected near ice divides [Martín et al., 2009a; Hofstede et al., 2013] by comparing measurements made at the same stake using different antenna orientations. However, we do not consider this further here. The result is many measured vertical velocity profiles per stake (1606 in total and ~7 per stake on average), each corresponding to a different combination of measurements taken during each deployment.

2.3. Numerical Ice Divide Flow Model

In section 3 we examine the results of a full-Stokes ice divide flow simulation to aid discussion of the Raymond Effect and the englacial velocity measurements. Figure 2 shows our idealized model geometry. The vertical and horizontal coordinates are y and x, respectively. Ice accumulates at a constant and uniform rate, a, at the surface of an ice sheet, which is frozen to the bed (no sliding occurs). The model does not include a firn layer. We follow Martín et al. [2009b] in solving the thermomechanically coupled Stokes equations using the finite-element package Elmer/Ice [Gagliardini et al., 2013]. We assume isotropic plane flow with a temperature-dependent power law Glen rheology with a flow law exponent n = 3. Ice flux boundary conditions at both lateral boundaries impose a plug flow out of the 14 km wide domain, which leads to an ice divide forming at a position determined by the pattern of accumulation rates and the relative magnitudes of the boundary fluxes. Ice temperature evolves according to the nonsteady heat equation. We prescribe a uniform temperature at the surface and a uniform geothermal flux, Q_G, at the base. We balance the total surface accumulation rate across the model domain with the total boundary flux to maintain a global mass balance. During simulations the age of the ice is tracked and the position of the ice surface changes in response to ice flow and accumulation. The domain is discretized into 400 horizontal elements and 40 vertical elements. Martín et al. [2009b] describes the details of the numerical methods.

3. Simulating Ice Divide Flow

Figure 3 plots results from a simulation of an ice sheet of thickness $H \approx 800$ m sitting on flat bedrock. Uniform surface accumulation ($a = 0.5 \text{ m a}^{-1}$) and equal flux boundary conditions at the margins impose a stationary ice divide at x = 0. The ice surface temperature is $T_s = -20$ °C and $Q_G = 50$ mW m⁻¹. The plots show the state of the system after it has reached a near-steady state (when the ice velocity, strain rate, and age fields in the upper 95% of the ice divide's thickness have stopped evolving), after a simulation time equal to 5 times the characteristic time.

$$\tau = H/a = 1600 a$$
.

Figures 3a and 3b show the two-dimensional distribution of vertical ice velocities and vertical strain rates. We focus on ice dynamics in the vertical dimension to compare with pRES observations. The plots depict the entire thickness of the ice divide and only the central region between x = -4 km and x = +4 km.

The Raymond Effect is evident in both plots. Considering the strain rates first (Figure 3b), deep ice beneath the divide deforms relatively slowly owing to the nonlinear stress dependence of the effective viscosity and the low deviatoric stress in this region caused by the small surface slope and frozen bed (Figures 3b and 3c). As surface accumulation is uniform and the system is quasi-steady, the total depth-integrated vertical strain rate is approximately the same in the flanks as it is at the divide (only approximately due to a small contribution to the

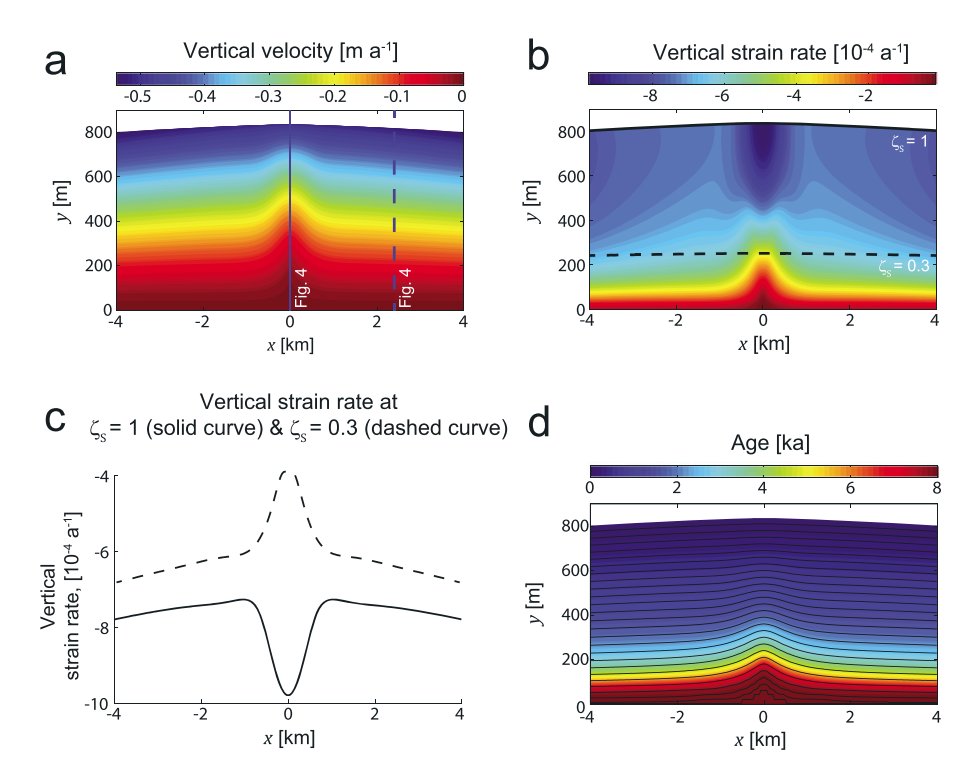


Figure 3. Simulated ice divide flow. Results of a two-dimensional ice divide flow simulation that has reached a quasi-steady state. (a) The two-dimensional spatial variation of vertical ice velocities over the full thickness of the ice divide and the central 8 km of the 14 km wide model domain. (b) The vertical strain rate in the same region. (c) Vertical strain rates extracted from the results along the ice surface, $\zeta_S = 1$, (solid curve) and at a normalized elevation $\zeta_S = 0.3$ (dashed curve). The surfaces $\zeta_S = 1$ and $\zeta_S = 0.3$ are indicated by the solid and dashed lines, respectively, in Figure 3b. (d) The age of the ice in the same region displayed in Figures 3a and 3b with isochrones displayed as black curves. Nonuniform age intervals between isochrones are chosen such that the curves are approximately equally spaced in the vertical coordinate.

vertical motion of the surface in the flanks from horizontal flow). Hence, to compensate for the slow deformation of the deep ice, near-surface ice beneath the divide deforms ~35% faster than near-surface ice in the flanks (solid curve in Figure 3c). The region of enhanced surface strain rates extends ±950 m (±1.2H) horizontally from the divide in each direction. This spatial variation in strain rates leads to an upwarping in the vertical velocity contours beneath the divide (Figure 3a) and a strong contrast between vertical velocity profiles at the divide and the flanks (blue curves in Figure 4). At all depths ice flows downward more slowly at the divide than in the flanks and the vertical velocity shape function (the vertical velocity normalized with surface accumulation; Figure 4) is more nonlinear—i.e., it is steeper near the surface and shallower at depth—at the divide than at the flanks.

Figure 3d shows how the age structure of the ice has been influenced by the Raymond Effect. Simulated isochrones (in black) are warped upward beneath the divide because ice flows downward more slowly in this region than in the flanks (Figure 4). These features are Raymond Arches. At any particular depth, ice beneath the divide is older than ice at the same depth beneath the flanks [Raymond, 1983].

In this steady isotropic simulation, the maximum in surface strain rates, the minimum in deep strain rates and the single Raymond Arches are all vertically aligned with the ice divide (Figure 3).

4. Measuring Ice Divide Flow

4.1. Vertical Velocity Profiles

The procedure described in section 2.1 pairs up radar returns from two pRES deployments, and the majority of these pairings successfully yield vertical ice velocity profiles through to the bed. However, we find that some pairs produce either very few velocity measurements or profiles with very steep gradients in velocity inconsistent with pulse-echo radargrams showing smoothly undulating layers. The reasons for these

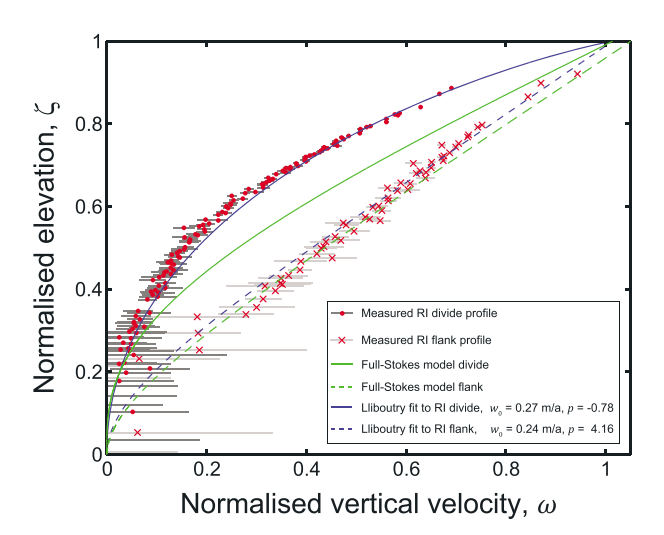


Figure 4. Comparison of measured and modeled vertical velocities. Measured velocity profiles from the divide and eastern flank of Roosevelt Island (normalized by w_s derived during Lliboutry fits) are shown as red points and crosses, respectively, with uncertainties indicated by the horizontal bars. Green curves are vertical velocity profiles normalized with the accumulation rate a extracted from the full-Stokes model solution (Figure 3). The modeled velocity at the surface in the flank is >1 due to a small contribution to vertical flow from horizontal motion. Blue curves are Lliboutry fits to the measured profiles also normalized with w_s . Dashed curves correspond to flank positions (at $x = \pm 2.4$ km in the model and at locations plotted in green and labeled in Figure 6b). Solid curves correspond to positions close to divides (at x = 0 km in the model and at locations plotted in green and labeled in Figure 6b).

erroneous measurements vary and are not completely understood. Sometimes a return will have an unusually high noise floor caused by user error, external interference, or significant variations in the temperature of the network analyzer during a measurement. This reduces the number of reflectors that can be used in velocity calculations, in particular near the bed where signals are strongly attenuated. In other cases, the algorithm that detects reflectors (section 2.1) can partially fail, leading to phase-unwrapping errors and unphysically steep gradients in measured velocities. Conducting repeat measurements during each deployment, to obtain many vertical velocity profiles for each stake, usually ensures that we obtain a sufficient number of robust velocity profiles at each location.

Figure 5 shows examples of vertical velocity profiles measured near the divides at each field site at locations indicated in green in Figures 1, 6a, 6b, 7a, and 7b. Profiles from Berkner Island, Roosevelt Island, and Fletcher Promontory extend to the bed. We identify bed reflectors using their strength relative to

their neighboring reflectors and, assuming stationary bedrock and a frozen ice sheet base, we uniformly offset the profiles to set the velocity at the bed to zero to obtain absolute vertical ice velocities. On Adelaide Island ice velocities were only reliably retrieved from depths <150 m and velocities are expressed relative to an arbitrary datum.

Measured vertical velocities do not vary linearly with depth (Figures 4 and 5). In particular, at near-divide locations the velocity changes more rapidly with depth near the surface than near the bed—i.e., the shallow ice deforms more rapidly than ice near the bed. Furthermore, near the surface, velocities incorporate the compaction rate of the firn, which is superimposed on the vertical velocity caused by horizontal stretching.

Two analytical approximations, often used to describe ice flow at divides for ice core dating, were derived by *Dansgaard and Johnsen* [1969] and *Lliboutry* [1979] [see *Martín and Gudmundsson*, 2012]. We examine how well each approximation can match our observations and use the Lliboutry function to calculate strain rates.

Dansgaard and Johnsen [1969] assumed that above a critical normalized elevation ζ_c horizontal ice velocity is constant and that it decreases linearly to zero between ζ_c and the bed. This corresponds to

$$w = \frac{w_s \zeta^2}{\zeta_c(2 - \zeta_c)}, \qquad 0 \le \zeta \le \zeta_c,$$

$$w = w_s \frac{2\zeta - \zeta_c}{2 - \zeta_c}, \qquad \zeta_c \le \zeta \le 1,$$
(1)

where w_s is the vertical velocity at the surface and w is the vertical velocity as it varies with the normalized elevation ζ . Using the Shallow Ice Approximation *Lliboutry* [1979] derived the following expression:

$$w = w_s \left(1 - \frac{p+2}{p+1} \zeta + \frac{1}{p+1} \zeta^{p+2} \right), \tag{2}$$

where *p* is an ice rheology parameter that determines the nonlinearity of the function [see also *Parrenin and Hindmarsh*, 2007; *Parrenin et al.*, 2007a, 2007b; *Martín and Gudmundsson*, 2012].

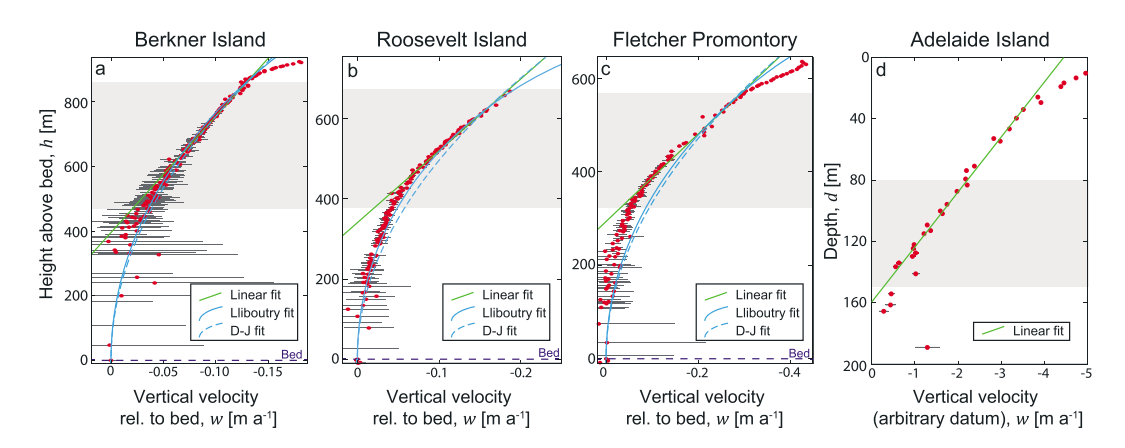


Figure 5. Examples of vertical velocity profiles measured with pRES at our four field sites: (a) Berkner Island, (b) Roosevelt Island, (c) Fletcher Promontory, and (d) Adelaide Island. Velocities in Figures 5a–5c are expressed relative to the bed where we assume zero velocity. Velocities in Figure 5d are relative to an arbitrary datum as we cannot detect the bed in pRES return from Adelaide Island. Linear near-surface fits are plotted as green curves, and nonlinear function fits are plotted as blue curves (solid curves are Lliboutry fits; dashed curves are Dansgaard-Johnsen (D-J) fits). The grey regions indicate that the depth ranges used in the linear fits and the horizontal grey lines represent measurement uncertainties. Where it can be detected in pRES returns, the bed depth is indicated by the horizontal blue dashed lines.

We perform nonlinear fits of both functions, weighted with the squared reciprocal of the uncertainties, to find optimal values for each pair of parameters (ζ_c and w_s ; p and w_s) corresponding to each velocity profile (blue solid and dashed curves; Figures 5a–5c). The functions approximately characterize variations in the shape of the velocity profiles, but neither function is able to completely capture the nonlinearity of the observations. This inability is most apparent in fits to profiles measured near divides (Figure 5). Later we discuss the implications of this for ice core dating.

To compare our observations with the full-Stokes model simulation (section 3), Figure 4 plots Lliboutry fits to profiles from Roosevelt Island (blue curves; Figure 4) and vertical velocity profiles extracted from the full-Stokes model results (green curves; Figure 4) with vertical velocity profiles measured at the divide and eastern flank of Roosevelt Island. The Lliboutry fits and the measured profile are normalized using w_s values derived during the fits and the modeled profiles are normalized with the accumulation rate. The solid lines correspond to near-divide profiles (Figures 5a and 5b), and the dashed lines correspond to flank profiles. The two pairs of curves and the two measured profiles show qualitatively similar variations in shape between the flanks and the divides. In the flanks, vertical gradients in the vertical velocity (i.e., vertical strain rates) are nearly uniform except near the bed where they reduce to zero (both the shape function and the model solution assume no basal melting or sliding). At the divides, as mentioned above, deformation is concentrated near the surface and deep ice deforms relatively slowly.

We do not expect an exact match between the measured profiles and the numerical model results, as we were not aiming to simulate a specific divide. Rather, the model simulates a generic ice divide with an arbitrary surface temperature and unrealistic [Lenaerts et al., 2014] uniform accumulation and bedrock topography. However, it is clear from Figure 4 that the numerical model fails to capture the nonlinearity of the measured divide profiles. Later we discuss if this is due to our use of Glen's flow law with n=3 to parameterize ice rheology.

4.2. Spatial Variation in Vertical Strain Rates

To examine spatial variations in ice flow, we extract strain rates from our measured vertical velocity profiles. Because strain rates calculated directly from the vertical velocity data are noisy, we smooth profiles by curve fitting and calculate strain rates from the fits. Initially, we focus on a near-surface zone from where vertical strain rates are extracted using a linear fit. We then use the Lliboutry function fits to map three-dimensional variations in vertical strain rates within Fletcher Promontory.

4.2.1. Near-Surface Vertical Strain Rates

Immediately beneath a region of enhanced vertical velocities associated with firn compaction (e.g., $565 \text{ m} \le h \le 635 \text{ m}$ and $0.9 \le \zeta \le 1$; Figure 5c) is a zone where vertical velocities decrease linearly with depth,

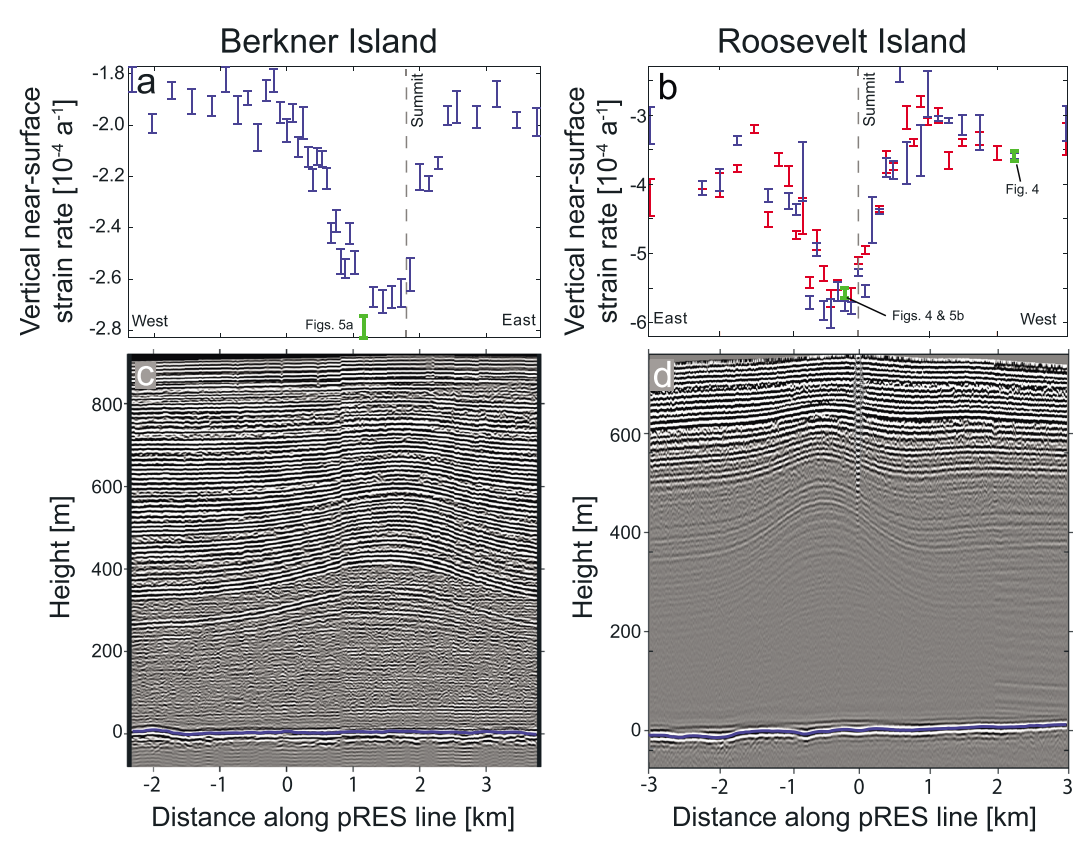


Figure 6. Results of radar surveys of Berkner Island and Roosevelt Island. (a and b) Near-surface strain rates calculated from linear fits to vertical velocity profiles (Figure 5). Data obtained from velocity profiles measured with the pRES antennas orientated parallel and perpendicular to survey lines are plotted in blue and red, respectively. Green data points near the divides correspond to the profiles displayed in Figures 4 and 5. The approximate locations of divide summits are shown by the vertical dotted lines. (c and d) Radar layer structure from pulse-echo radar surveys (Figure 1), linearly projected on to the pRES survey lines. The bed reflector is shown in blue.

indicating uniform vertically compressive strain rates (shown in grey in Figure 5). Figures 6 and 7 plot near-surface vertical strain rates estimated from the slope of weighted linear least squares fits to each velocity profile in the near-surface zone. These are plotted above pulse-echo radargrams (blue lines; Figure 1) that reveal the radar layer architecture within each divide. For every linear fit we use the depth of the bottom of the firn layer (80 m; estimated as the lowest depth at which nonlinear velocities associated with firn compaction are visible in velocity profiles) as one limit on the depth range of velocity measurements used in the fit. For the other limit we use a normalized elevation $\zeta = 0.5$ with data from Berkner Island, Roosevelt Island, and Fletcher Promontory and a depth of 150 m with data from Adelaide Island (approximately the depth to which velocity measurements were consistently retrieved at this site). Results from Berkner Island, Roosevelt Island, and Adelaide Island are displayed in full, while for Fletcher Promontory only results from the stakes indicated in yellow in Figure 1c are displayed.

For clarity, from each pRES stake we only plot the strain rate with the lowest uncertainty (as calculated during least squares fitting). However, we treat pRES measurements conducted using different antenna orientations separately, so from field surveys where both antenna orientations were used two strain rates are plotted for each stake, shown in red and blue. This clarifies the plots and removes erroneous data associated with the issues highlighted at the start of section 4. The strain rate patterns we discuss below can still be seen in the data (although less clearly) when all the data are plotted together. One alternative approach is to plot the weighted average of the strain rates calculated from all the pairs of measurements from each stake. Another alternative is to discard data that corresponds to fitting parameters that lie outside some range that we consider to be plausible. We have explored each alternative and have found that the qualitative pattern of vertical strain rates that we discuss below is not affected.

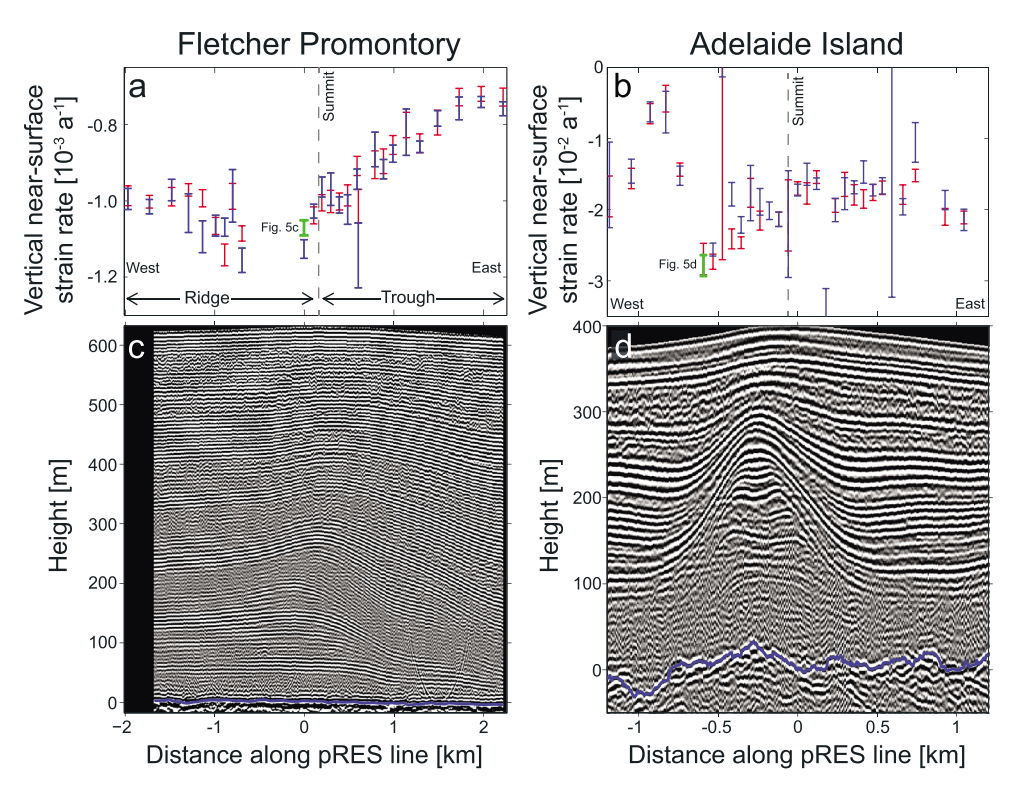


Figure 7. (a–d) Results of radar surveys of Fletcher Promontory and Adelaide Island. Layout is identical to Figure 6. The green data points correspond to the profiles plotted in Figures 5c and 5d. For Fletcher Promontory only data from stakes indicated in yellow in Figure 1c are plotted.

The results from Berkner Island and Roosevelt Island (Figure 6) conform to the predictions of ice divide flow theory. Near-surface strain rates are more compressive at the divides than in the flanks (\sim 40% higher at Berkner Island and \sim 90% higher at Roosevelt Island). These regions of enhanced near-surface compression, extending from the divide \pm 1.2 km (\pm 1.3H) at Berkner Island and \pm 0.9 km (\pm 1.1H) at Roosevelt Island, are similar in horizontal extent to such regions simulated by our full-Stokes model (Figure 3).

Pulse-echo radargrams linearly projected on to the Berkner Island and Roosevelt Island pRES lines are displayed in Figures 6c and 6d. Stacks of Raymond Arches visible in these data are approximately vertically aligned with their corresponding ice divides and maxima in the magnitude of near-surface strain rates.

Results from the Fletcher Promontory triple junction (Figures 7a and 7c) also reveal a close association between surface topography, radar layer structure, and near-surface strain rates. This subset of the survey bisects the triple junction, running along one of its ridges, through its summit (where the three divides meet) and along an interridge trough (Figure 1c). Near-surface strain rates (Figure 7a) are ~25% higher in magnitude beneath the ridge and the summit than in the trough. The maximum in this magnitude is approximately vertically aligned with the stack of Raymond Arches visible in the radargram displayed in Figure 7c. This can be understood by extending ideas highlighted by our two-dimensional modeling (section 3) to the three-dimensional flow within the triple junction. Where surface slopes are low beneath the summit and the ridges, the Raymond Effect causes deep ice to stiffen and flow more slowly than ice at depth in the troughs. Near-surface ice deforms relatively rapidly to compensate [Gillet-Chaulet and Hindmarsh, 2011]. Furthermore, modeling predicts that a nonzero surface slope along an ice divide suppresses the Raymond Effect [Martín et al., 2009b], so we expect to observe larger magnitude strain rates at the summit, where the surface slope is very small, than beneath the ridges, where the surface slopes away from the summit (Figure 1c). This expectation is fulfilled by our observations (Figure 7a).

Strain rates measured on Adelaide Island (Figure 7b) do not exhibit the Raymond Effect. Near-surface strain rates are negative everywhere (except for four outliers with large uncertainties, not displayed), but the data are noisier and lack the maximum in magnitude near the divide. Although strain rate magnitudes in the western

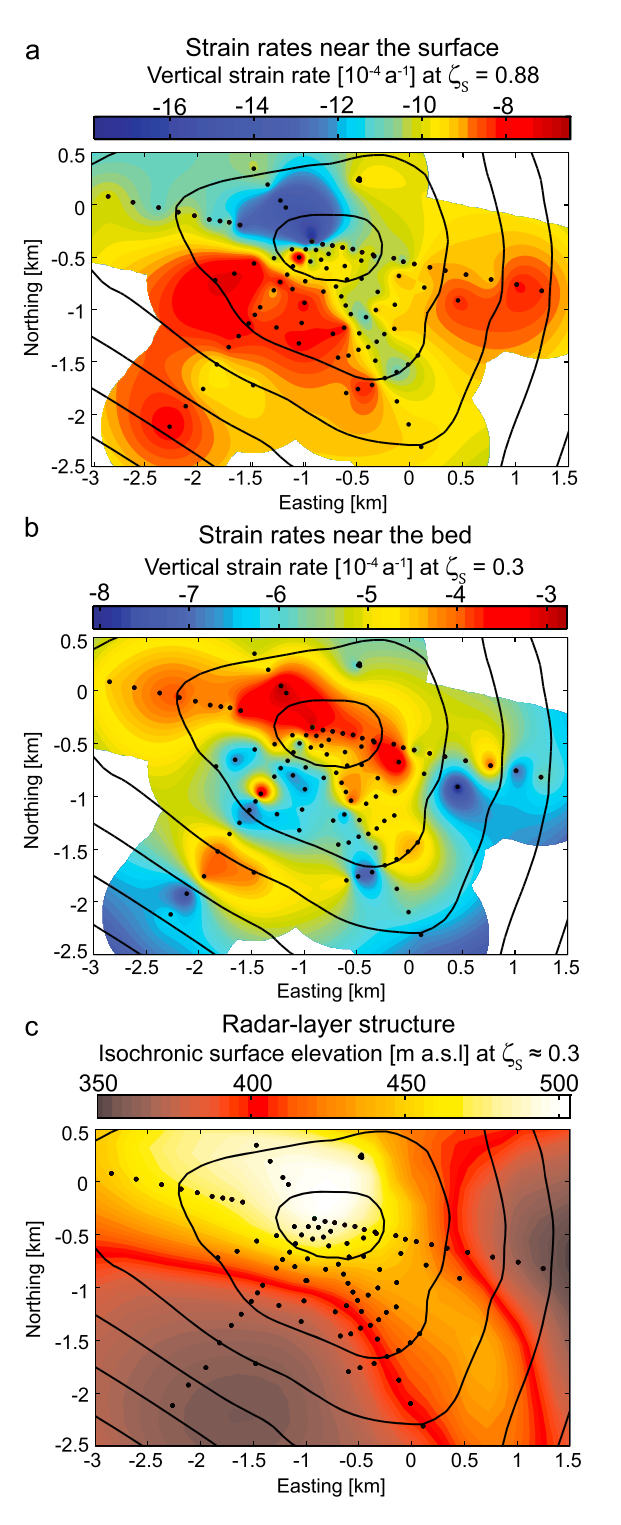


Figure 8. Fletcher Promontory's three-dimensional strain rate and radar layer structure. Vertical strain rates calculated using Lliboutry function fits to measured vertical velocity profiles (e.g., blue curve in Figure 5c) (a) near the surface, but beneath the firn ($\zeta_S = 0.88$), and (b) near the bed ($\zeta_S = 0.3$). (c) The approximate elevation of a deep isochronous surface at a mean normalized elevation $\zeta_S \approx 0.3$ observed using pulse-xecho radar [*Hindmarsh et al.*, 2011]. Data are projected polar stereographically with latitude of true scale 71°S. Coordinates are aligned to the polar stereographic grid but expressed relative to a local origin.

flank are lower than at the divide, this is not the case in the eastern flank. Later we discuss whether this is due to problems with detecting reflectors at Adelaide Island or if the dynamics of the divide are more complex than the idealized steady scenario simulated in section 3.

4.2.2. Vertical Variation in Strain Rate Patterns

For each vertical velocity profile we estimate vertical strain rates at a series of normalized elevations ζ_S from the gradients of the corresponding Lliboutry fits. For the Fletcher Promontory data we use these estimates to interpolate strain rate surfaces, two of which are visualized in Figure 8 with a map of the observed elevation of an englacial layer at a mean normalized elevation of $\zeta_s \approx 0.3$ [Hindmarsh et al., 2011]. Figure 8a shows strain rates estimated at ζ_S = 0.88, and Figure 8b shows strain rates estimated at $\zeta_S = 0.3$. Note that an alternative approach is to smooth profiles with a low-pass filter before differentiating to calculate strain rates. The results of this procedure are qualitatively the same as the results presented below. Note also that in section 4.1 we showed that the Lliboutry parameterization is unable to fully capture the nonlinearity of vertical velocity profiles, particularly near divides. Therefore, the interpolated strain rate surfaces derived from these fits will underrepresent the true concentration of deformation near the surface beneath divides.

When interpolating between nonstructured strain rate data to compute these surfaces we use radial basis functions [Hindmarsh et al., 2011]. Our pRES surveys produced multiple velocity profiles per survey stake and multiple corresponding strain rate data points. To produce a single-valued interpolated surface, we first omit velocity profiles that produce $w_s < 0.3 \, \mathrm{m \ a^{-1}}$ or $w_s > 0.6 \, \mathrm{m \ a^{-1}}$, then we choose the strain rate data from each stake derived from the profile with the lowest root-mean-square uncertainty. Qualitatively, the spatial variations in strain rate are independent of the details of this procedure.

The spatial variation of near-surface strain rates revealed by Figure 8a is similar to that discussed above with reference to Figure 7a.



The magnitudes of the near-surface strain rates are relatively high at the ridges and highest at the summit. Lower magnitude strain rates are measured beneath the interridge troughs. As expected from the form of the profiles in Figure 5 and equation (2), the inverse pattern is seen lower down at $\zeta_S = 0.3$ (Figure 8b); the magnitudes of deep strain rates are lower beneath the divides than beneath the troughs. This is the first time deep strain rates have been measured in such high spatial resolution and over such a large area near a divide, and the data clearly show the Raymond Effect in action.

Figure 8c shows how the Raymond Effect has affected radar layer structure. The deep layer depicted has been deformed into an elliptical cupola with its apex located slightly to the north of the summit [Hindmarsh et al., 2011]. The cupola is located in the region where we directly measure the slow deformation of deep ice caused by the Raymond Effect.

As expected from Figure 6a, calculating deep strain rates from Lliboutry fits to the Berkner Island data produces a similar strain rate pattern near the bed—lower strain rates at the divide compared to the flanks. The pattern cannot be seen in the Roosevelt Island data because a significant number of the velocity profiles suffer from phase-unwrapping errors discussed at the beginning of section 4.1, which erroneously introduce large velocity gradients, particularly deeper in the ice where the signal-to-noise ratio is lower.

5. Discussion

Ice flow variations mapped at Berkner Island, Roosevelt Island, and Fletcher Promontory validate the predictions of a full-Stokes ice flow model that simulates the Raymond Effect. However, although the model qualitatively matches observations, simulated divide velocity profiles are more linear than measured profiles; the deformation observed with pRES is faster near the surface and slower near the bed than simulated deformation. This is significant because although we did not match the model with site-specific surface temperatures and accumulation rates, in theory, the shape of vertical velocity profiles is relatively insensitive to variations in such environmental conditions [Wilchinsky and Chugunov, 1997; Martín et al., 2009b]. Another factor that we did not include in the model is variability in bed topography. This may significantly affect ice dynamics, but the beds beneath Berkner Island, Roosevelt Island, and Fletcher Promontory, where we obtained full-depth velocity profiles, are relatively flat (Figures 6 and 7) [Hindmarsh et al., 2011]. Therefore, variable bed topography seems unlikely to account for the mismatch between the shapes of modeled and observed vertical velocity profiles.

In the model we used Glen's flow law with n=3 to parameterize ice rheology. Using a similar model Gillet-Chaulet et al. [2011] needed to increase n to 4.5 to match observations of near-surface strain rates in Greenland. Future work using our more extensive data set could investigate if the match between modeled and measured velocities can be improved by increasing n or by using an alternative flow law parameterization to include, for example, ice anisotropy or a yield stress.

Fitting measured vertical velocity profiles with two analytical ice flow approximations [Dansgaard and Johnsen, 1969; Lliboutry, 1979] show that neither approximation is able to fully capture the nonlinearity of vertical velocity profiles observed at divides. Both approximations have been used by previous authors to date ice cores drilled at divides [e.g., Dansgaard et al., 1993; Hondoh et al., 2004; Parrenin et al., 2007a, 2007b; Martín and Gudmundsson, 2012], so our findings may have implications for the accuracy of these dating efforts. For example, the age predicted by a one-dimensional age model at a depth of 550 m beneath the Roosevelt Island divide, varies by around 33% depending on whether the model is driven by a Dansgaard-Johnsen velocity profile (with model parameters $w_s = 0.23 \,\mathrm{m~a^{-1}}$ and $\zeta_c = 0.97$, optimized during the fit; Figure 5b) or by our measured velocities (Figure 5b).

Spatial strain rate variations measured on Adelaide Island do not clearly conform to the predictions of our steady state ice flow simulation. Is this due to technical problems with obtaining measurements or are this divide's dynamics more complex than those we simulated?

We cannot reliably detect radar reflectors below about 150 m at Adelaide Island using pRES. This could be due to attenuation caused by high impurity concentrations and relatively high ice temperatures [MacGregor et al., 2007] as is expected due to the island's oceanic, low-latitude setting, or the failure of the algorithm that detects and matches reflectors between radar returns caused by high reflector displacements (section 2.1).



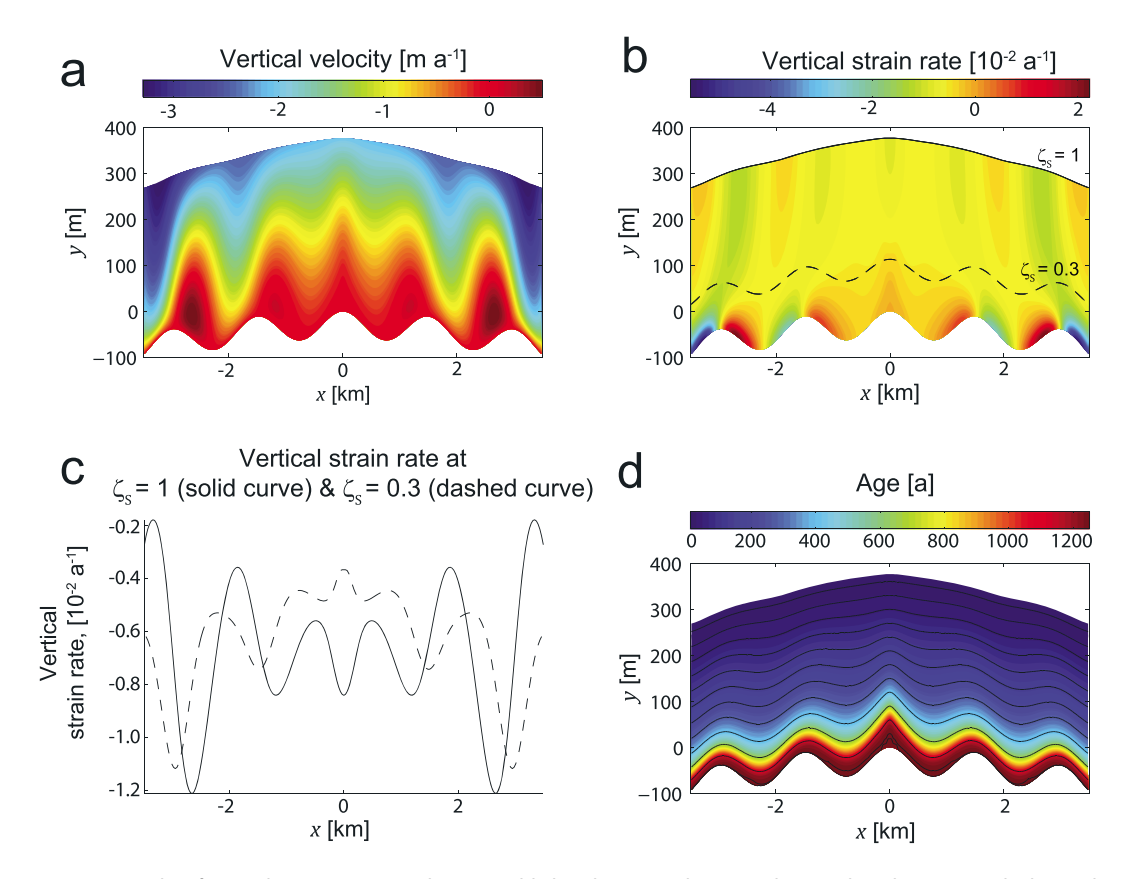


Figure 9. Results of a simulation using a synthetic variable basal topography created to emulate the topography beneath the divide on Adelaide Island (Figure 1d) that has reached a quasi-steady state. Color maps display (a) vertical velocity, (b) vertical strain rate, and (d) age. (c) The vertical strain rate at the surface (solid curve) and at a normalized depth of $\zeta_S = 0.3$ (dashed curve).

As a consequence some velocity profiles are derived from sparse data, which could contribute to the apparently anomalous calculations of near-surface strain rates. However, near-surface strain rates calculated from velocity profiles obtained using different antenna orientations often agree within measurement uncertainties (cf. red and blue data points; Figure 7b), suggesting that the measurements could reflect real complexity in flow at Adelaide Island.

Our pulse-echo survey on Adelaide Island (partially displayed in Figure 7d) reveals bedrock undulations with amplitudes \sim 60 m and wavelengths of 1–2 km. As ice moves away from the divide it flows over these undulations. To simulate the ice-dynamic effect of these undulations, we construct a synthetic representation of Adelaide Island's bed topography and simulate ice divide flow over it using our ice flow model (section 2), while prescribing an accumulation rate, an initial ice thickness and a surface temperature appropriate for Adelaide Island ($a = 2 \text{ m a}^{-1}$, $H \approx 400$, $T_s = -8^{\circ}\text{C}$).

Figure 9 displays results from the 1250 year (\sim 6r) simulation. The bedrock undulations strongly influence vertical velocities and strain rates. Near the bed each undulation, except the one immediately beneath the divide, is associated with a downstream region of enhanced vertical compression (Figure 9b) and an upstream region of vertical extension (Figure 9b) and upward ice flow (Figure 9a). An associated horizontally alternating pattern of increased and decreased vertical compression extends upward to the ice surface (Figure 9c) and is superimposed on the familiar pattern of strain rate variations caused by the Raymond Effect. The Raymond Effect still operates, and a Raymond Arch still forms (Figure 9d), but of the two factors impacting surface strain rates—the Raymond Effect and the flow over bedrock undulations—the bedrock undulations are the most significant.

If uneven bed topography influences ice dynamics, so dramatically this could mask the Raymond Effect in the near-surface strain rate measured using pRES. Divide migration, spatial variations in accumulation,



ice fabric, and the three-dimensional effect of bedrock undulations can also impact ice divide dynamics significantly. Future modeling could investigate if realistic combinations of these factors can account for the complexity of the Adelaide Island observations.

6. Summary

We have described the first surface-based technique capable of remotely measuring the vertical velocity of ice through to the beds of ice sheets. We have applied it at several ice divides and obtained the most comprehensive observations to date of a nonlinear fluid-dynamical phenomenon called the Raymond Effect, qualitatively validating theoretical predictions of the dynamics of ice divides. Previous studies using englacial instruments have obtained similar measurements [e.g., Perutz, 1949; Raymond et al., 1994; Hawley et al., 2002; Zumberge et al., 2002; Elsberg et al., 2004], but our technique allows us to map vertical ice velocities in unprecedented spatial resolution. For example, three-dimensional variations in vertical strain rates were mapped using velocity profiles measured at >120 locations on Fletcher Promontory covering an area >10 km². Such a comprehensive survey was possible because each profile is derived from two radar measurements which each take about 5 min to complete.

Using our unique data set, we have shown that neither a full-Stokes model (when it employs a typical Glen ice rheology with n = 3) nor two analytical ice flow approximations [Dansgaard and Johnsen, 1969; Lliboutry, 1979] can fully capture the nonlinearity of ice divide vertical velocity profiles. Similar conclusions regarding the failure of simple models to describe ice divide flow have been reached before [e.g., Pettit and Waddington, 2003; Martín et al., 2006; Gillet-Chaulet et al., 2011; Martín and Gudmundsson, 2012], but in the future our high-resolution englacial velocity data can be used to better constrain ice rheology and improve model-based ice core chronologies.

Acknowledgments

Logistical support for the work on Fletcher Promontory, Adelaide Island, and Berkner Island was provided by many members of the British Antarctic Survey's field operations team. Logistical support for the Roosevelt Island work was provided by Antarctica New Zealand (K049) and the U.S. Antarctic Program. This work was supported by the British Antarctic Survey's Polar Science for Planet Earth program and two standard grants from the UK's National Environmental Research Council: NE/F00446X/1 "Measuring and modelling the Raymond Effect for to infer low strain rate ice rheology" and NE/J008087/1 "Dating and modelling fast ice sheet grounding-line retreat over the last 4000 years in the SW Weddell Sea, Antarctica." The work on Roosevelt Island was funded by the U.S. National Science Foundation (ANT-0944307). This is a contribution to the Roosevelt Island Climate Evolution (RICE) Programme. funded by contributions from New Zealand, Australia, Denmark, Germany, Italy, the People's Republic of China, Sweden, United Kingdom, and the U.S. Data published in this article can be obtained by contacting the corresponding author directly. We thank Martin Truffer, Reinhard Drews, and two anonymous reviewers for comments that have greatly improved the manuscript.

References

- Conway, H., B. L. Hall, G. H. Denton, A. M. Gades, and E. D. Waddington (1999), Past and future grounding-line retreat of the West Antarctic Ice Sheet, Science, 286(5438), 280-283, doi:10.1126/science.286.5438.280.
- Corr, H. F., A. Jenkins, K. W. Nicholls, and C. S. M. Doake (2002), Precise measurement of changes in ice-shelf thickness by phase-sensitive radar to determine basal melt rates, Geophys. Res. Lett., 29(8), 73-1-74-1, doi:10.1029/2001GL014618.
- Dansgaard, W., and S. J. Johnsen (1969), A flow model and a time scale for the ice core from Camp Century, Greenland, J. Glaciol., 8, 215–223. Dansgaard, W., H. B. Clausen, N. Gundestrup, C. U. Hammer, S. F. Johnsen, P. M. Kristinsdottir, and N. Reeh (1982), A new Greenland deep ice core, Science, 218(4579), 1273-1277, doi:10.1038/364218a0.
- Dansgaard, W., et al. (1993), Evidence for general instability of past climate from a 250-kyr ice-core record, Nature, 364(6434), 218-220. Drews, R., C. Martin, D. Steinhage, and O. Eisen (2013), Characterizing the glaciological conditions at Halvfarryggen ice dome, Dronning Maud Land, Antarctica, J. Glaciol., 59(213), 9-20, doi:10.3189/2013JoG12J134.
- Elsberg, D. H., W. D. Harrison, M. A. Zumberge, J. L. Morack, E. C. Pettit, E. D. Waddington, and E. Husmann (2004), Depth-and time-dependent vertical strain rates at Siple Dome, Antarctica, J. Glaciol., 50(171), 511-521, doi:10.3189/172756504781829684.
- Fretwell, P., et al. (2013), Bedmap2: Improved ice bed, surface and thickness datasets for Antarctica, Cryosphere, 7(1), 375-393, doi:10.5194/tc-7-375-2013.
- Gagliardini, O., et al. (2013), Capabilities and performance of Elmer/Ice: A new generation ice-sheet model, Geosci. Model Dev., 6(1), 1299-1318, doi:10.5194/gmd-6-1299-2013.
- Gillet-Chaulet, F., and R. C. A Hindmarsh (2011), Flow at ice-divide triple junctions: 1. Three-dimensional full-Stokes modeling, J. Geophys. Res., 116, F02023, doi:10.1029/2009JF001611.
- Gillet-Chaulet, F., R. C. A. Hindmarsh, H. F. Corr, E. C. King, and A. Jenkins (2011), In-situ quantification of ice rheology and direct measurement of the Raymond Effect at Summit, Greenland using a phase-sensitive radar, Geophys. Res. Lett., 38, L24503, doi:10.1029/2011GL049843.
- Haran, T., J. Bohlander, T. Scambos, and M. Fahnestock (2005), MODIS Mosaic of Antarctica (MOA) Image Map, Natl. Snow and Ice Data Center, Boulder, Colo.
- Hawley, R. L., E. D. Waddington, D. L. Morse, N. W. Dunbar, and G. Zielinski (2002), Dating firn cores by vertical strain measurements, J. Glaciol., 48(162), 401-406, doi:10.3189/172756502781831250.
- Hindmarsh, R. C. A., E. C. King, R. Mulvaney, H. F. Corr, G. Hiess, and F. Gillet-Chaulet (2011), Flow at ice-divide triple junctions: 2. Three-dimensional views of isochrones architecture from ice-penetrating radar surveys, J. Geophys. Res., 116, F02024, doi:10.1029/2009JF001622.
- Hofstede, C., O. Eisen, A. Diez, D. Jansen, Y. Kristoffersen, A. Lambrecht, and C. Mayer (2013), Investigating englacial reflections with vibro-and explosive-seismic surveys at Halvfarryggen ice dome, Antarctica, Ann. Glaciol., 54(64), 189-200, doi:10.3189/2013AoG64A064.
- Hondoh, T., H. Shoji, O. Watanabe, E. A. Tsyganova, A. N. Salamatin, and V. Y. Lipenkov (2004), Average time scale for Dome Fuji ice core, East Antarctica, Polar Met. Glaciol., 18, 1-18.
- Hvidberg, C. S. (1996), Steady-state thermomechanical modelling of ice flow near the centre of large ice sheets with the finite-element technique, Ann. Glaciol., 23, 116-123.
- Jenkins, A., H. F. Corr, K. W. Nicholls, C. L. Stewart, and C. S. M. Doake (2006), Interaction between ice and ocean observed with phase-sensitive radar near an Antarctic ice-shelf grounding line, J. Glaciol., 52, 325-346, doi:10.3189/172756506781828502.
- Lenaerts, J. T. M., et al. (2014), High variability of climate and surface mass balance induced by Antarctic ice rises, J. Glaciol., 60(224), 1101-1110, doi:10.3189/2014JoG14J040.
- Lliboutry, L. A. (1979), A critical review of analytical approximate solutions for steady state velocities and temperature in cold ice sheets, Gletscherkd. Glazialgeol., 15(2), 135-148.



- MacGregor, J. A., D. P. Winebrenner, H. Conway, K. Matsuoka, P. A. Mayewski, and G. D. Clow (2007), Modeling englacial radar attenuation at Siple Dome. West Antarctica. using ice chemistry and temperature data. *J. Geophys. Res.*, 112, F03008. doi:10.1029/2006JF000717.
- Martín, C., and G. H. Gudmundsson (2012), Effects of nonlinear rheology, temperature and anisotropy on the relationship between age and depth at ice divides, *The Cryosphere*, 6(3), 1221–1229, doi:10.5194/tc-6-1221-2012.
- Martín, C., R. C. A. Hindmarsh, and F. J. Navarro (2006), Dating ice flow change near the flow divide at Roosevelt Island, Antarctica, by using a thermomechanical model to predict radar stratigraphy, *J. Geophys. Res.*, 111, F01011, doi:10.1029/2005JF000326.
- Martín, C., G. H. Gudmundsson, H. D. Pritchard, and O. Gagliardini (2009a), On the effects of anisotropic rheology on ice flow, internal structure, and the age-depth relationship at ice divides, *J. Geophys. Res.*, 114, F04001, doi:10.1029/2008JF001204.
- Martín, C., R. C. A. Hindmarsh, and F. J. Navarro (2009b), On the effects of divide migration, along-ridge flow, and basal sliding on isochrones near an ice divide, *J. Geophys. Res.*, 114, F02006, doi:10.1029/2008JF001025.
- Martín, C., R. Mulvaney, G. H. Gudmundsson, and H. Corr (2014), Inferring paleo-accumulation records from ice-core data by an adjoint method: Application to James Ross Island's ice core, Clim. Past Discuss., 10, 3821–3845, doi:10.5194/cpd-10-3821-2014.
- Nereson, N. A., and C. F. Raymond (2001), The elevation history of ice streams and the spatial accumulation pattern along the Siple Coast of West Antarctica inferred from ground-based radar data from three inter-ice-stream ridges, *J. Glaciol.*, 47(157), 303–313, doi:10.3189/172756501781832197.
- Nereson, N. A., and E. D. Waddington (2002), Isochrones and isotherms beneath migrating ice divides, *J. Glaciol.*, 48(160), 95–108, doi:10.3189/172756502781831647.
- Nye, J. F., M. V. Berry, and M. E. R. Walford (1972), Measuring the change in thickness of the Antarctic ice sheet, *Nature*, 240(97), 7–9, doi:10.1038/physci240007a0.
- Parrenin, F., and R. C. A. Hindmarsh (2007), Influence of a non-uniform velocity field on isochrone geometry along a steady flowline of an ice sheet, *J. Glaciol.*, 53(183), 612–622, doi:10.3189/002214307784409298.
- Parrenin, F., et al. (2007a), The EDC3 chronology for the EPICA Dome C ice core, Clim. Past, 3(3), 485–497, doi:10.5194/cp-3-485-2007.
- Parrenin, F., et al. (2007b), 1-D-ice flow modelling at EPICA Dome C and Dome Fuji, East Antarctica, Clim. Past, 3(2), doi:10.5194/cp-3-243-2007.
- Perutz, M. F. (1949), Direct measurement of the velocity distribution in a vertical profile through a glacier, J. Glaciol., 1(5), 249–249.
- Pettit, E. C., and E. D. Waddington (2003), Ice flow at low deviatoric stress, *J. Glaciol.*, 49(166), 359–369, doi:10.3189/172756503781830584. Pettit, E. C., H. P. Jacobson, and E. D. Waddington (2003), Effects of basal sliding on isochrones and flow near an ice divide, *Ann. Glaciol.*, 37(1), 370–376, doi:10.3189/172756403781815997.
- Pettit, E. C., T. Thorsteinsson, H. P. Jacobson, and E. D. Waddington (2007), The role of crystal fabric in flow near an ice divide, *J. Glaciol.*, 53(181), 277–288, doi:10.3189/172756507782202766.
- Pettit, E. C., E. D. Waddington, W. D. Harrison, T. Thorsteinsson, D. Elsberg, J. Morack, and M. A. Zumberge (2011), The crossover stress, anisotropy and the ice flow law at Siple Dome, West Antarctica, J. Glaciol., 57(201), 39–52, doi:10.3189/002214311795306619.
- Price, S. F., H. Conway, and E. D. Waddington (2007), Evidence for late Pleistocene thinning of Siple Dome, West Antarctica, *J. Geophys. Res.*, 112. F03021, doi:10.1029/2006JF000725.
- Raymond, C. F. (1983), Deformation in the vicinity of ice divides, J. Glaciol., 29(103), 357-373.
- Raymond, C. F., J. C. Rogers, P. L. Taylor, and B. Koci (1994), Vertical strain measurement in core holes, *Mem. Natl. Inst. Polar Res. Special issue*, 49, 234–240.
- Rignot, E., and J. Mouginot (2012), Ice flow in Greenland for the international polar year 2008–2009, *Geophys. Res. Lett.*, 39, L11501, doi:10.1029/2012GL051634.
- Rignot, E., J. Mouginot, and B. Scheuchl (2011), Ice flow of the Antarctic ice sheet, *Science*, 333(6048), 1427–1430, doi:10.1126/science 1208336
- Vaughan, D. G., H. F. Corr, C. S. Doake, and D. Waddington (1999), Distortion of isochronous layers in ice revealed by ground-penetrating radar, *Nature*, 398(6725), 323–326, doi:10.1038/18653.
- Wilchinsky, A. V., and V. A. Chuqunov (1997), Modelling ice-divide dynamics by perturbation methods, J. Glaciol., 43(144), 352–358.
- Zumberge, M. A., D. H. Elsberg, W. D. Harrison, E. Husmann, J. L. Morack, E. C. Pettit, and E. D. Waddington (2002), Measurement of vertical strain and velocity at Siple Dome, Antarctica, with optical sensors, *J. Glaciol.*, 48(161), 217–225, doi:10.3189/172756502781831421.